# Evolution of microstructure and residual stress during annealing of austenitic and ferritic steels

Roman Wawszczak, Andrzej Baczmanski, Marianna Marciszko, Miroslaw X. Wróbel, Tomasz Czeppe, Krzysztof Sztwiertnia, Chedly Braham, Katarzyna Berent

# Evolution of microstructure and residual stress during annealing of austenitic and ferritic steels

R. Wawszczak [a], A. Baczmański [a,*], M. Marciszko [a], M. Wróbel [b], T. Czeppe [c], K. Sztwiertnia [c], C. Braham [d], K. Berent [e]

[a] AGH—University of Science and Technology, WFiIS, al. Mickiewicza 30, 30-059 Kraków, Poland
[b] AGH—University of Science and Technology, WIMIP, al. Mickiewicza 30, 30-059 Kraków, Poland
[c] Institute of Metallurgy and Materials Science, Polish Academy of Sciences, ul. Reymonta 25, 30-059 Kraków, Poland
[d] PIMM, UMR 8006, Arts et Métiers ParisTech (ENSAM), 151 Bd de l'Hôpital, 75013 Paris, France
[e] AGH—University of Science and Technology, ACMIN, al. Mickiewicza 30, 30-059 Kraków, Poland

A B S T R A C T

In this work the recovery and recrystallization processes occurring in ferritic and austenitic steels were studied. To determine the evolution of residual stresses during material annealing the nonlinear $sin^2\psi$ diffraction method was used and an important relaxation of the macrostresses as well as the microstresses was found in the cold rolled samples subjected to heat treatment. Such relaxation occurs at the beginning of recovery, when any changes of microstructure cannot be detected using other experimental techniques. Stress evolution in the annealed steel samples was correlated with the progress of recovery process, which significantly depends on the value of stacking fault energy.

*Keywords:*
Residual stresses
X-ray diffraction
Microstructure
Recovery
Recrystallization
Crystallographic texture

## 1. Introduction

One of the characteristics which determine the strength of materials and their susceptibility to cracking is the state of residual stresses, i.e., the stresses between the parts of the externally unloaded component which remain after a process. The residual stress is generated during cooling of the cast metal or as a result of mechanical working of the polycrystalline materials, e.g., cold forming [1–3]. For example, during cold rolling the differences in irreversible plastic deformation of the surface layer and the interior of the sheet cause the incompatibility between these two volumes and leads to creation of a residual stress. Both value and heterogeneity of residual stresses significantly influence the fatigue characteristics and strength of materials. If added to the externally applied loads, residual stresses can lead to the destruction, but can also be advantageous for the fatigue life, of the product. A compressive stress state in the surface layer reduces the risk of cracking or/and decoupling of the applied coating. In contrast, the tensile stress can initiate and accelerate the development of cracks and damage of the coating. A variety of surface treatments can be applied to improve the mechanical properties of materials, by generating compressive surface stress state (e.g., laser treatment, ball peening, sand blasting or burnishing of the surface).

In polycrystalline materials residual stresses can be divided into three categories according to their spatial extent and origin [2,4]. The macrostresses (the first order stress $\sigma^I_{ij}$), caused by heterogeneity of the material or process, extend over the largest distances — ranging from tenths of millimeters to centimeters or more. In the unloaded sample, these stresses compensate themselves over the entire volume, and their heterogeneity in the sample depends on the history of the treatment. The principal stresses in the direction of rolling and/or transverse direction (*RD* and *TD*, respectively), usually present on the rolled sample surface, may be an example. The type of these stresses (compressive or tensile) and their values depends on the rolling conditions, e.g., friction between the rolls and the material.

The difference between the stress value in a particular grain and the first order value is defined as the second order stress $\sigma^{II}_{ij}$. The variation of stress state from grain to grain is caused by differences in irreversible deformations of the crystallites during thermal or mechanical treatment. The intergranular stresses, also called mismatch stresses or microstresses, can arise from differences in thermal expansion coefficients or plastic deformation between grains. The sum of the second order stresses for all crystallites in a sufficiently large volume is equal to zero.

* Corresponding author.
*E-mail address:* Andrzej.Baczmanski@fis.agh.edu.pl (A. Baczmański).

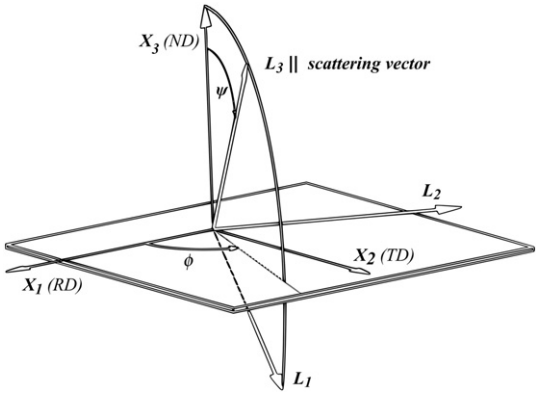


**Fig. 1.** Orientation of the laboratory system ***L***, defined by the direction $L_3$ of the scattering vector and direction $L_2$ lying on the sample surface, with respect to the sample coordinates $X_1$, $X_2$ and $X_3$ coincided with *RD*—rolling direction, *TD*—transverse direction and *ND*—normal direction, respectively. Orientation of the scattering vector in relation to the sample frame is given by the $\phi$ and $\psi$ angles.

Stresses of the third order ($\sigma_{ij}^{III}(\mathbf{r})$) describes stress variation in the smallest scale, i.e., within the single grain. They result from the stress field existing around the dislocations, or from disorder in the regular crystal lattice near to the boundary of a single grain or mosaic structures.

The stress at a given point of the material (i.e., at position r) is equal to the sum of all the above-defined components, namely:

$$\sigma_{ij}(\mathbf{r}) = \sigma_{ij}^{I} + \sigma_{ij}^{II} + \sigma_{ij}^{III}(\mathbf{r}) \tag{1}$$

A comprehensive review of the literature on the recovery process and recrystallization is given by Humphreys and Hatherly [5], where such effects of thermal treatment as evolution of dislocation density, crystallographic texture, resistivity, and grain size of polycrystalline metals are presented. The novelty of the present study is to investigate the relaxation of macroscopic residual stress (first order stresses) and the plastic strain mismatch (second order stresses) as a function of temperature and correlate this process with the other changes taking place during the recovery process. Obtaining the original results was possible using a nonlinear $sin^2\psi$ method proposed and described in details by Baczmański et al. [6–8], and applied in other works [9–11]. The study was performed for the ferritic and austenitic steels. At first, all samples were deformed by cold rolling, and subsequently subjected to isothermal annealing at different temperatures, until recrystallization.

## 2. Stress determination methodology

X-ray diffraction is often used to measure residual stresses in polycrystalline materials [1–3]. In this work the multireflection $sin^2\psi$ diffraction method is applied to determine the interplanar spacings $<d(\phi,\psi)>_{\{hkl\}}$ for a few reflections *hkl* and for various orientations of the scattering vector relative to the sample frame. These orientations are described by two angles $\phi$ and ψ, as shown in Fig. 1. Finally, the equivalent lattice parameters $<a(\phi,\psi)>_{\{hkl\}} = <d(\phi,\psi)>_{\{hkl\}}\sqrt{h^2+k^2+l^2}$ are calculated from measured interplanar spacings. The methodology is described in detail in literature [6–12].

To analyze the relations $<a(\phi,\psi)>_{\{hkl\}}$ vs. $sin^2\psi$ the nonlinear $sin^2\psi$ method allowing separation of the macro- and plastic incompatibility residual stresses is used [6–9]. In this method the theoretical second order stresses, generated during plastic deformation, are calculated using the elastoplastic model. However, the evolution of the stress magnitude resulting from the work hardening and the annealing induced relaxation cannot be exactly predicted. Therefore, the dependence of the incompatibility stresses on the grain orientation are calculated by the model, while the amplitude of the theoretical stresses are scaled by an adjusting factor *q*. This factor relates the predicted values $\overline{\sigma_{ij}^{IIg(pi)}}$ of the incompatibility stresses to the actual ones $\sigma_{ij}^{IIg(pi)}$ [6–9], i.e.:

$$\sigma_{ij}^{IIg(pi)} = q\ \overline{\sigma_{ij}^{IIg(pi)}}. \tag{2}$$

Then, the equivalent lattice parameter $<a(\phi,\psi)>_{\{hkl\}}$ measured by diffraction for given angles $\phi$ and $\psi$ can be expressed through the first order stresses $\sigma_{ij}^{I}$ and the predicted second order stresses $\overline{\sigma_{ij}^{IIg(pi)}}$:

$$<a(\phi,\psi)>_{\{hkl\}} = \left[F_{ij}\mathrm{hkl},\phi,\psi\,\sigma_{ij}^{I} + q<\gamma_{3m}\gamma_{3n}s_{mnij}^{g}\overline{\sigma_{ij}^{IIg(pi)}}>_{\{hkl\}}\right] a^{o} + a^{o}, \tag{3}$$

where: $s_{mnij}^{g}$ are the elastic constants of a single crystal defined relatively to the sample coordinate system ***X***, $\gamma_{km}$ are the transformation matrix from the sample frame ***X*** to the laboratory system ***L*** (Fig. 1), $a^o$ is the lattice parameter of the stress free material and $F_{ij}(hkl,\phi,\psi)$ are the X-ray stress factors (*XSF*) calculated from the $s_{mnij}^{g}$ elastic constants and the measured textures (described by *ODFs* — orientation distribution functions) [6–9].

In the nonlinear $sin^2\psi$ the calculated $<a(\phi,\psi)>_{\{hkl\}}$ values (according to Eq. (3)) are fitted to the measured ones. To this end, a least square procedure is applied and, as the result, the adjusting parameters, i.e., $\sigma_{ij}^{I}$, *q* and $a^o$ are determined. Finally, by using *q* factor in Eq. (2), the values of plastic incompatibility stresses $\sigma_{ij}^{IIg(pi)}$ in the real sample can be calculated from the model values $\overline{\sigma_{ij}^{IIg(pi)}}$ [6–9]. Therefore, both the first order and the second order stresses ($\sigma_{ij}^{I}$ and $\sigma_{ij}^{IIg(pi)}$) are determined for the studied volume of the material.

In the present work, stress analysis will be performed for the plastically deformed (cold rolled samples) as well as those samples subjected to the annealing treatment. It is assumed that during annealing the stresses are partly or entirely released, and during the process of relaxation the magnitude of the $\sigma_{ij}^{IIg(pi)}$ stresses decreases but their orientation dependence remains unchanged. Therefore, the theoretical values of the $\overline{\sigma_{ij}^{IIg(pi)}}$ obtained from the elastoplastic model can also be used to determine the second order stresses in the annealed samples [13].

As described above, the stresses state in the material can be studied by diffraction with the help of the elastoplastic deformation models, in which the deformation process is considered at two different scales, i.e., for a particular grain and for a polycrystalline aggregate. The scale transition model must be used in calculations to relate the local processes with the behavior of the polycrystalline material. At the grain scale, the plastic deformation is caused by the glides on the crystallographic planes. According to Schmid's criterion, a given slip system (characterized by the plain and direction of glide) is active only when the resolved shear stress on this system is equal to its critical value $\tau_c$. Because of the multiplication of dislocations during plastic deformation, the slip systems are hardened (i.e. the value of $\tau_c$ increases). This process is described in calculations using the work hardening matrix, whose

**Table 1**
The chemical composition of the studied steels (wt.%).

| | C | Si | Mn | P | S | Cu | Ni | Cr | Mo | Al | Fe |
|---|---|---|---|---|---|---|---|---|---|---|---|
| Ferritic steel | 0.002 | 0.012 | 0.105 | – | – | – | – | 0.016 | – | 0.058 | Balance |
| Austenitic stainless steel 316L | 0.02 | 0.056 | 1.67 | 0.04 | 0.04 | 0.35 | 11.14 | 17.24 | 1.96 | – | Balance |

**Table 2**
Diffraction conditions used in the measurement of stress and crystallographic texture.

| Material | Anode of X-ray tube | Wavelength $\lambda_{K\alpha1}/\lambda_{K\alpha2}$ (Å) | Reflections hkl for texture measurement | Reflections hkl for stress measurement | Scattering angle $2\theta$ (°) for $\lambda_{K\alpha1}$ |
|---|---|---|---|---|---|
| | | | 110 | – | 68.6 |
| | | 2.289726 | 200 | 200 | 105.8 |
| Ferritic steel | Cr | 2.293651 | 211 | 211 | 155.2 |
| Austenitic | Mn | 2.101854 | 111 | – | 61.0 |
| stainless steel | | 2.105822 | 200 | – | 71.7 |
| | | | 220 | 220 | 111.8 |
| | | | – | 311 | 151.8 |

components relate the rate of the critical resolve shear stress (CRSS) for the $s$-th system ($\dot{\tau}_c^s$) to the rate of the plastic slip ($\dot{\gamma}^t$) on the $t$-th active system [14], i.e.: $\dot{\tau}_c^s = \sum_t H^{st}\dot{\gamma}^t$ (where the derivative $\frac{\partial}{\partial t}$ is denoted by a dot). In the present work an isotropic linear hardening is assumed, i.e., the hardening matrix components are equal to the same constant value: $H^{st} = H$.

The plastic deformation at the scale of grain level is related to the macroscopic deformation of the polycrystalline aggregate using the scale transition model, in which the concentration tensors $\boldsymbol{A}$ or/and $\boldsymbol{B}$ are introduced. Using these tensors the local strain rate $\dot{\varepsilon}_{ij}$(or stress rate $\dot{\sigma}_{ij}$) of a grain can be related to the macrostrain rate $\dot{E}_{kl}$(or macrostress rate $\dot{\Sigma}_{kl}$), i.e.:

$$\dot{\varepsilon}_{ij} = A_{ijkl}\dot{E}_{kl} \quad \text{or} \quad \dot{\sigma}_{ij} = B_{ijkl}\dot{\Sigma}_{kl} \tag{4}$$

The concentration tensor (tensors $\boldsymbol{A}$ or $\boldsymbol{B}$) can be determined for an ellipsoidal inclusion representing grain embedded in the homogeneous matrix. The mechanical properties of the matrix are calculated as the average for all polycrystalline grains. To determine the localization tensors, macroscopic and local behavior of polycrystals, we have applied a self-consistent homogenization scheme elaborated by Lipinski et al. [15–16] and extended by Zattarin et al. [17].

Another scale transition model was proposed by Leffers [18] and extended by Wierzbanowski [19,20]. In this method (called the *LW* model) the stress rate of a grain $\dot{\sigma}_{ij}$ is related to the macroscopic stress rate of polycrystalline aggregate $\dot{\Sigma}_{ij}$ through the equation, i.e.:

$$\dot{\sigma}_{ij} = \dot{\Sigma}_{ij} + L^*_{ijkl}\left(\dot{E}_{kl} - \dot{\varepsilon}_{kl}\right) \tag{5}$$

where $L^*_{ijkl}$ is the Hill's constraint tensor.

The second term of Eq. (5) describes the evolution of intragranular stresses generated by the incompatibilities of the grains to the surrounding aggregate. To do this, the Hill's constraint tensor $L^*_{ijkl}$ is used [17,19,20]. In this approach it is assumed that the differences between the grain deformation $\varepsilon_{kl}$ and the macroscopic deformation $E_{kl}$ of the sample lead to the creation of the incompatibility stresses. In the *LW* model, the Hill's $L^*_{ijkl}$ tensor is usually represented by the elastic shear modulus $\mu_e$ multiplied by the elastoplastic accommodation parameter $\alpha$, i.e.:

$$\begin{aligned} L^*_{ijkl} &= \alpha\mu_e u_{ij} \quad \text{for } ij = kl \\ L^*_{ijkl} &= 0 \qquad \text{for } ij \neq k \end{aligned} \tag{6}$$

where: $\alpha$ value determines the effect of accommodation of a grain incompatibility ($\alpha$ can be changed from zero to infinity), while $u_{ij}$ (assumed to be equal 0 or 1) is used to describes the anisotropy of grains interaction.

## 3. Materials studied and their characterization

Two series of cold rolled steel samples were prepared and subjected to isothermal annealing at different temperatures. The chemical composition of the investigated steels is shown in Table 1. The low-carbon ferritic steel was cold rolled up to of 85% reduction in thickness and isothermally annealed for 30 min under $CO_2 + CO$ atmosphere at temperatures: 100 °C, 200 °C, 400 °C, 600 °C and 800 °C. The austenitic stainless steel (AISI 316L) was cold rolled to the reduction of 70%, and then annealed in an atmosphere of argon for 120 min at temperatures: 400 °C, 450 °C, 500 °C, 600 °C, 650 °C, 850 °C and 1170 °C.

Preliminary X-ray studies were performed on a PANalytical X'Pert diffractometer using Cu radiation ($\lambda_{K\alpha1}$ = 1.54060 Å and $\lambda_{K\alpha2}$ = 1.54443 Å). A Göbel mirror collimating the incident beam and a parallel collimator (Soller slits) placed in front of a scintillation detector were used in the measurements. The diffraction patterns obtained for the cold rolled materials show that each of the studied steels contains a

**Table 3**
Single crystal elastic constants and parameters used to calculate stress factors $F_{ij}$ and to predict elastoplastic deformation.

| Material | Critical resolved shear stress $\tau_0$ (MPa) — initial value | Hardening parameter $H$ (MPa) | Self consistent model | | | Model LW | |
|---|---|---|---|---|---|---|---|
| | | | Single crystal elastic constants (used also to calculate $F_{ij}$) (GPa) [24,25] | | | Shear modulus $\mu_e$ (GPa) | Elastoplastic accommodation matrix $u_{ij}$ |
| | | | $C_{11}$ | $C_{12}$ | $C_{44}$ | | |
| Ferritic steel | 200 | 80 | 231 | 134.4 | 116.4 | not used | not used |
| Austenitic stainless steel | 200 | 80 | 197.5 | 124.5 | 122 | 80 | $u_{13} = u_{31} = 0$<br>$u_{ij} = 1$ *for other indexes ij* |

**Table 4**
Stress determined using free-surface stress factors for the studied materials. Plastic mismatch stresses were calculated by a self-consistent model for ferrite and LW model for austenite.

| Material | First order stress (MPa) | | | | | Mean second order plastic incompatibility stress $\sigma_{eq}^{Ilg(pi)}$ (MPa) (von Mises measure Eq. (7)) |
|---|---|---|---|---|---|---|
| | $\sigma^I_{11}$ | $\sigma^I_{22}$ | $\sigma^I_{12}$ | $\sigma^I_{13}$ | $\sigma^I_{23}$ | |
| Ferritic steel | −124.0 ± 2.5 | −30.4 ± 3.1 | −8.7 ± 2.6 | −4.1 ± 1.1 | −0.7 ± 1.0 | 59.2 ± 2.5 |
| Austenitic stainless steel | −38.7 ± 6.3 | −70.0 ± 7.9 | −19.9 ± 5.5 | −4.1 ± 2.0 | −0.7 ± 1.7 | 81.8 ± 8.1 |

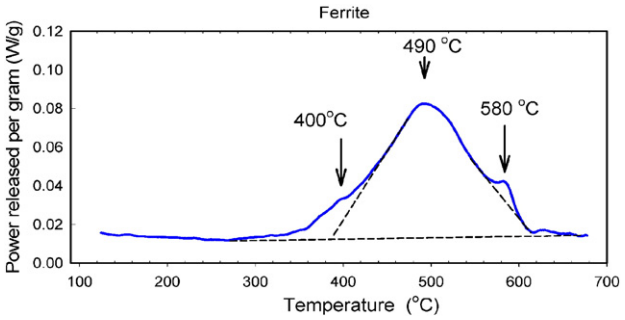


**Fig. 2.** *DSC* signal showing the dependence of heat release vs. temperature for the cold rolled ferritic steel (85% reduction) during continuous heating with the rate of 20 K/min.

single phase, and only a small contribution of martensite was found in the austenitic stainless steel.

An X-ray Seifert diffractometer with a chromium tube (for the ferrite) and a manganese tube (for the austenite) was used to analyze the stresses and the crystallographic texture (c.f. Table 2). The radiation wavelengths were selected taking into account both the minimum fluorescence of iron and the highest possible accuracy of the lattice strains measurement (a sufficiently large angle of scattering $2\theta$ decreases the uncertainty of the strain measurement [1–3]). The point-focused beam formed by a circular-shaped collimator with a diameter of 1.5 mm was applied to measure textures and stresses. The orientation of the samples with respect to the scattering vector was changed using a table enabling rotations described by $\psi$ and $\phi$ angles (Fig. 1). To avoid surface effects (i.e., texture and strain heterogeneity near the surface) a layer with a thickness of 200 μm was removed from each specimen by electropolishing.

To determine crystallographic texture, the pole figures were measured for $\psi$ angle in the range between 0° and 65° and for $\phi$ angle between 0° and 360°, with an increment of 5° for both $\psi$ and $\phi$ angles, as defined in Fig. 1 (these angles correspond respectively to the rotations $\alpha$ and $\beta$ usually used for the Euler cradle and to the description of a pole figure [21]). The *ODFs* were calculated from the pole figures {110}, {200}, {211} measured for the ferrite and from the pole figures {111}, {200}, {220} measured for the austenite. The analysis of the experimental data was done using the *WIMV* procedure [22].

Reflections 200, 211 and 220, 311 were used respectively to measure the lattice strains in the ferritic steel and in the austenitic stainless steel (Table 2). The measurements were conducted for the fixed values of the angle $\phi$, equal to 0°, 30°, 60°, 90°, 180°, 210°, 240° and 270° for the ferritic sample, while in the case of austenite $\phi$ angle was equal to 0°, 45°, 90°, 180°, 225° and 270°. For each value of $\phi$, the $\psi$ angle was varied in the range of $sin^2\,\psi$ from 0 up to 0.8. In the analysis of experimental data, the background was approximated by a linear function and subtracted from the recorded peaks. Then, the peak profiles ($K_{\alpha 1}$ and $K_{\alpha 2}$ doublet) were matched by the pseudo-Voigt function [23] and the interplanar distances $<d(\phi, \psi)>_{\{hkl\}}$were calculated from the peak position by

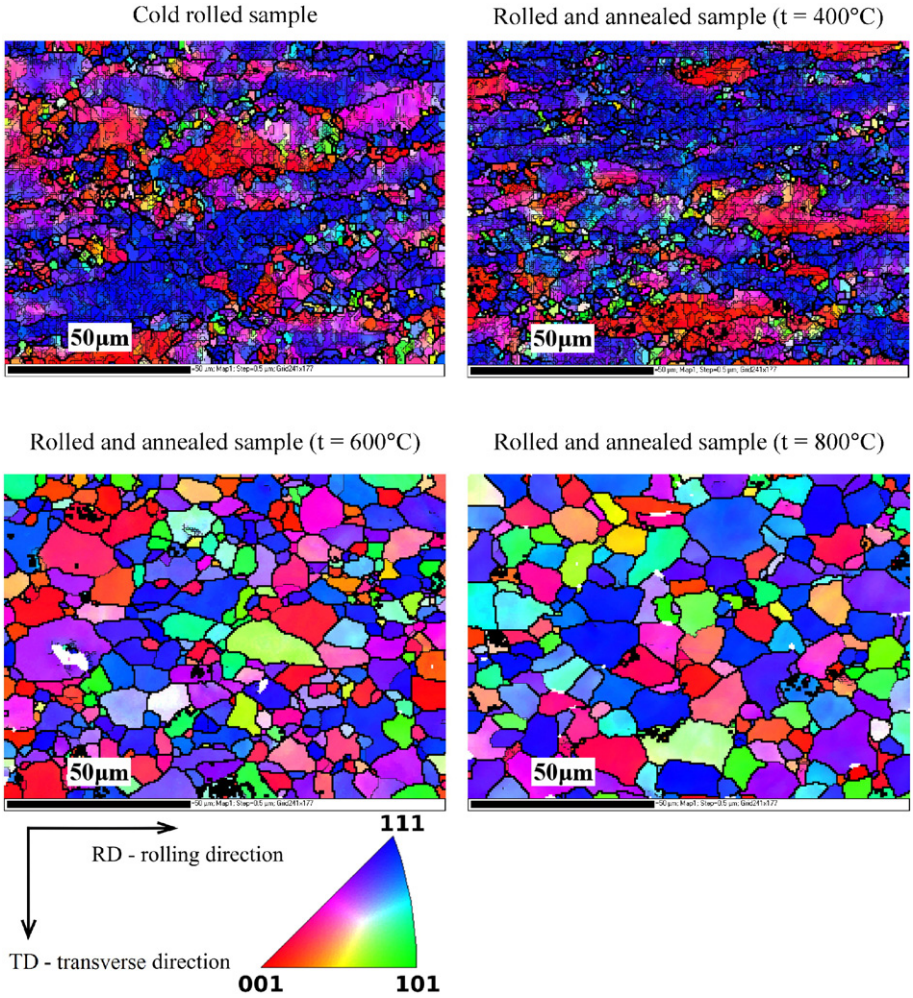


**Fig. 3.** Maps of orientations supplied by *EBSD* technique for the cold rolled (reduction of 85%) and rolled and annealed ferritic steel. The legend shows the basic orientation triangle with colors assigned to the different orientations of the direction normal to the sample surface.

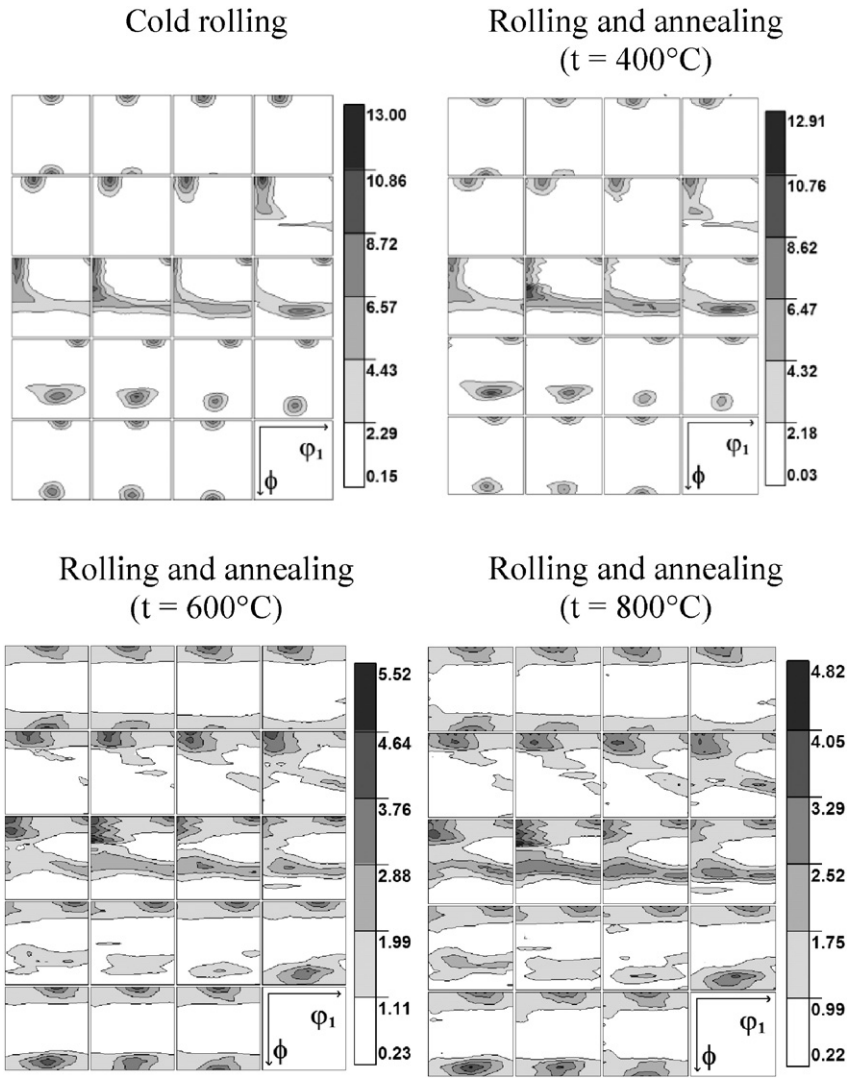


**Fig. 4.** Orientation distribution function for the ferrite subjected to rolling and annealing at various temperatures (sections through Euler space, displaced with an interval of 5° along axis $\varphi_2$ are shown [21]).

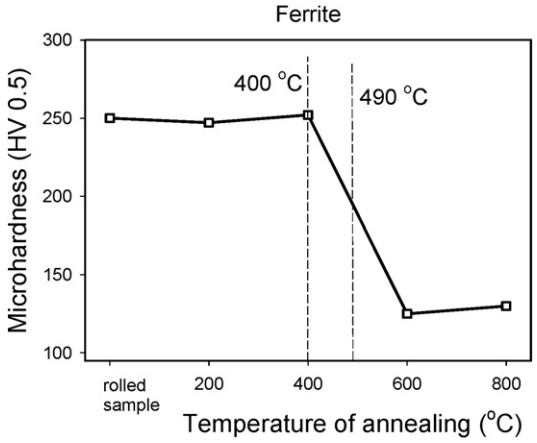


**Fig. 5.** Vickers microhardness measured for samples of ferritic steel cold rolled and annealed at different temperatures. The dashed lines depict characteristic temperatures found in the calorimetric measurements, c.f. Fig. 2.

applying Bragg's law. Finally, the mean equivalent lattice parameters $<a(\phi, \psi)>_{\{hkl\}}$ were determined for the given *hkl* reflections and different sets of $\phi$ and $\psi$ angles defining scattering vector orientations (c.f. Fig. 1).

To analyze the nonlinear $<a(\phi, \psi)>_{\{hkl\}}$ vs. $sin^2\psi$ curves, firstly the nonlinearities observed on these plots and caused by plastic incompatibility stresses must be predicted by the model. As mentioned in the used method, only the amplitude of nonlinearities is scaled by the *q* factor according to Eq. (3). To this end, the model calculations were carried out assuming plastic deformation on the <110>{111} slip systems for the *f.c.c.* structure (austenite) and on the <111>{110} and <111>{112} slips for the *b.c.c.* structure (ferrite). The model simulation of elastoplastic deformation was performed for a set of $10^6$ grains with orientations determined from the crystallographic textures measured for the cold rolled samples. Using a least square fitting procedure, based on Eq. (3), the macrostress (i.e. the first order stress $\sigma^I_{11}$ and $\sigma^I_{22}$) and *q* factor were determined (it was assumed that $\sigma^I_{33} = 0$ due to relaxation of forces normal to the surface layer penetrated by X-rays). In the fitting procedure the free-surface X-ray factors $F_{ij}$ [8] calculated from elastic constants of single crystal (Table 3) and experimental *ODFs* were used. Next, the second order stresses $\sigma_{ij}^{IIg(pi)}$ were computed from Eq. (2). Due to differences in grains interactions (for details see

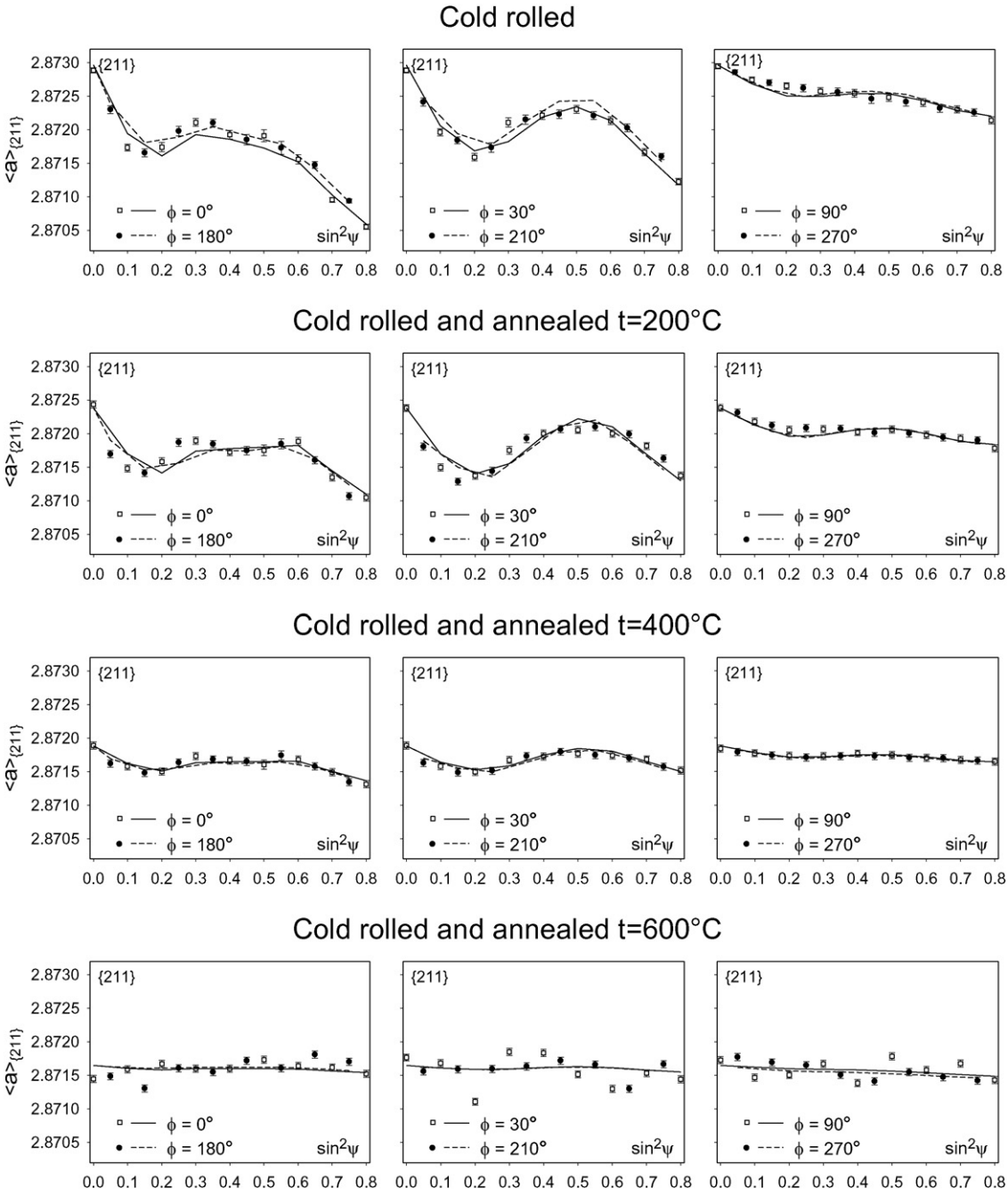


**Fig. 6.** The results of fitting theoretical lines to experimental plots ($<a(\phi,\psi)>_{\{hkl\}}$ vs. $sin^2\psi$) for ferritic steel samples which were cold rolled to a reduction of 85% and annealed at different temperatures (nonlinear $sin^2\psi$ method). The results for 211 reflection are shown.

[13]) the best fit of the predicted plots to the measured equivalent parameters $<a(\phi, \psi)>_{\{hkl\}}$ was obtained when the self-consistent model was used for the ferritic and the *LW* model was applied for the austenitic samples. The model parameters are given in Table 3, while the determined stresses are collated in Table 4. In the case of second order stress, the mean equivalent von Mises stress $\sigma_{eq}$ was calculated for all grains using the formula:

$$\sigma_{eq} = \left[\frac{1}{2}\left\{(\sigma_{11}-\sigma_{22})^2 + (\sigma_{11}-\sigma_{33})^2 + (\sigma_{22}-\sigma_{33})^2\right\} + 3\left\{(\sigma_{12})^2 + (\sigma_{13})^2 + (\sigma_{23})^2\right\}\right]^{\frac{1}{2}} \quad (7)$$

## 4. Evolution of microstructure and stresses during annealing

This section presents the results of residual stress and microstructure studies performed for cold rolled steels subjected to annealing at different temperatures.

### 4.1. Ferritic steel

The calorimetric measurements in the temperature range 120 °C–680 °C were conducted for the cold rolled ferritic steel using the DuPont 910 *DSC* — differential scanning calorimeter. In the second part of experiment, the series of isothermally annealed samples were prepared for the microstructural and X-ray studies. Microstructures at the samples' surfaces were investigated on the scanning electron microscope (Philips

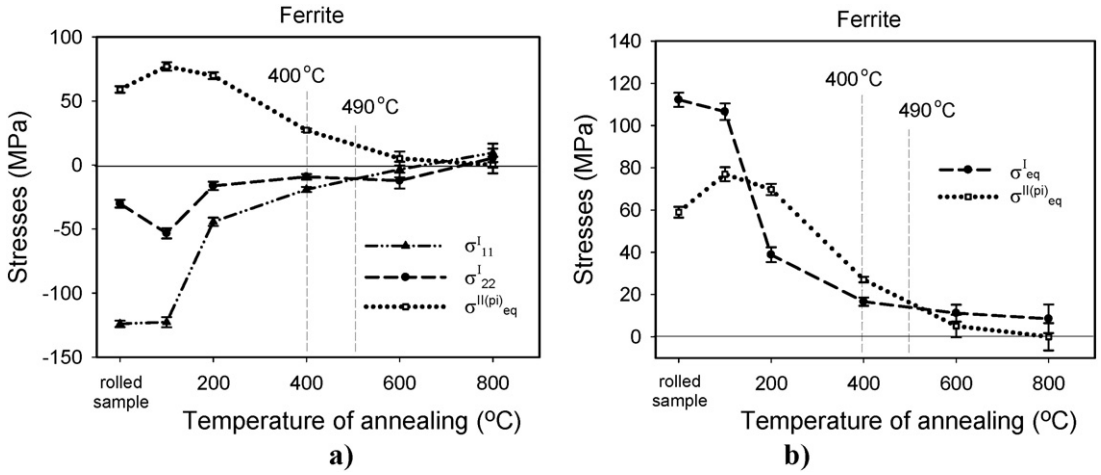


**Fig. 7.** Dependence of residual stress on temperature for samples of ferritic steel cold rolled to a reduction of 85%: a) components of the first order macrostress $\sigma^{I}_{ii}$ and the average von Mises plastic mismatch stress $\sigma^{IIg(pi)}_{eq}$, b) von Mises stresses calculated for the first ($\sigma^{I}_{eq}$) and the mean plastic incompatibility ($\sigma^{IIg(pi)}_{eq}$) stresses.

XL 30) using the electron back scattering diffraction (*EBSD*) technique. Subsequently, the Vickers microhardness was measured in accordance with the ASTM E-384 Test Method, and finally the crystallographic textures and the residual stresses were determined from X-ray diffraction measurements, using the methodology described in Refs. [6–9].

*4.1.1. Calorimetric measurements*

The dependence of heat released by the cold rolled ferritic steel sample versus temperature during constant heating with the rate of 20 K/min are shown in Fig. 2. One large exothermic thermal effects on the *DSC* curve is visible between 360 °C and 600 °C. The effect reveals a composed structure with the main maximum at 490 °C and two additional low maxima at about 400 °C and 580 °C. All the pronounced exothermic effect should be related to the recrystalization and grains' growth processes, with the kinetic maximum at 490 °C and completely finished at about 600 °C. It can be noticed that at the beginning of this exothermic process the released heat slowly increases with temperature, which may be related to the ordering of the crystal lattice defects during the recovery process (300 °C–400 °C).

*4.1.2. EBSD measurements*

The lattice orientations of the grains were determined at the nodes of a grid with cell size 0.5 μm ∗ 0.5 μm, using the *EBSD* technique for the series of ferritic samples (cold rolled and isothermally annealed during 30 min at different temperatures). Selected crystallographic orientation maps are shown in Fig. 3, where the orientations of the normal to the rolled sheet with respect to the crystal frame are presented. The thicker lines represent so-called wide-angle boundaries separating grains with lattice misorientation greater than or equal to 15°, while the thin lines are drawn for low angle boundaries of subgrains with misorientation of crystallographic lattice in the angular range: 2°–15°. Analyzing Fig. 3, it can be concluded that directly after plastic deformation the studied material contains a large number of relatively small subgrains, and the grains are elongated along the rolling direction (*RD*).

The microstructure does not change significantly after annealing at temperatures lower than 400 °C, i.e., the heat release starting from a temperature of 300 °C, observed during the calorimetric measurement, can be related to the recovery process. Distinct changes of the microstructure in the annealed samples are visible after annealing at a temperature of 600 °C, when the sample was completely recrystallized. This agrees with the ending temperature of recrystallization determined by the calorimetry and no significant changes in the microstructure were noticed after annealing at a temperature of 800 °C. The dimensions of the recrystallized grains do not exceed several tens of a micrometer. It should be noted that in spite of the fact that isothermal processes proceed in a different way than during constant heating rate experiments, the temperature ranges determined with *DSC* experiments agree well with the above-presented *EBSD* results.

*4.1.3. Crystallographic texture*

Fig. 4 provides the *ODFs* for cold rolled and subsequently annealed samples calculated from pole figures measured using the Cr X-ray tube (see Table 2) [13]. The obtained result proves that the texture did not change for an annealing temperature up to 400 °C, while significant

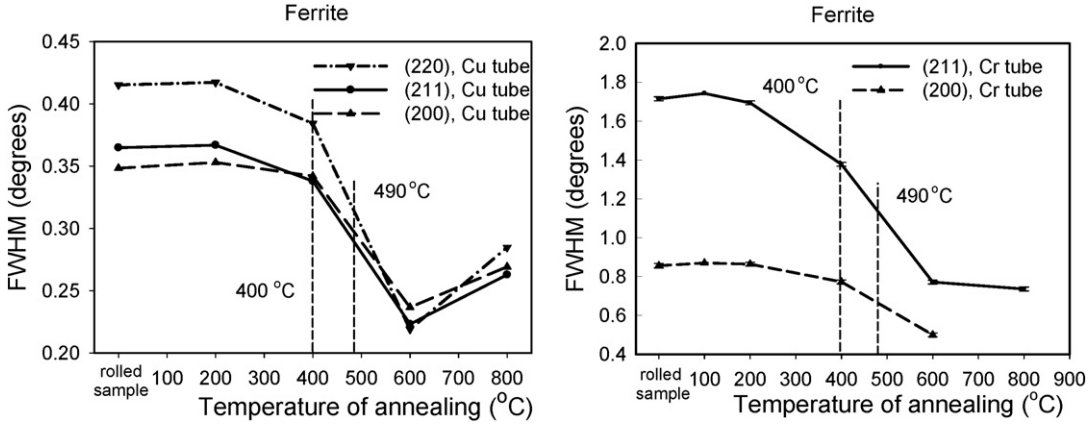


**Fig. 8.** Changes of peak widths versus temperature of annealing for the ferritic steel samples.

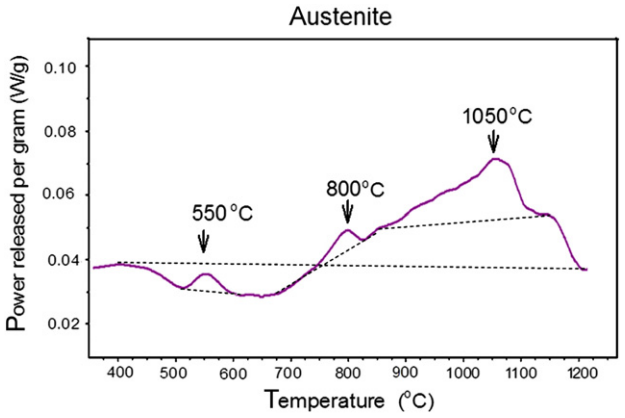


**Fig. 9.** The dependence of heat release vs. temperature for the austenitic stainless steel cold rolled up to a reduction of 70%. Continuous heating with the rate of 10 K/min was applied.

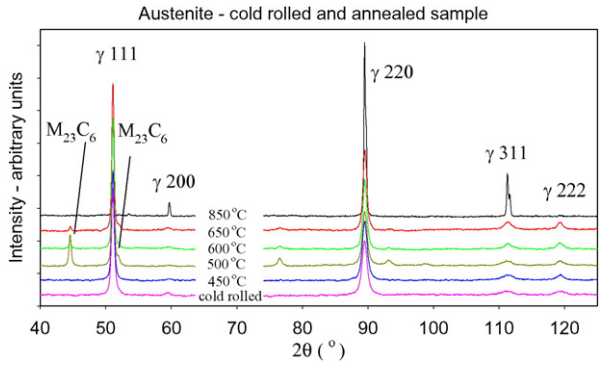


**Fig. 11.** Diffractograms obtained for cold rolled austenitic stainless steel after isothermal annealing for 120 min at different temperatures. An X-ray tube with a Co anode ($\lambda_{K\alpha1} = 1.78897$ Å and $\lambda_{K\alpha2} = 1.79285$ Å) was used.

changes are observed only for the samples annealed at temperatures of 600 °C and 800 °C, i.e., after recrystallization. This is consistent with the results of the calorimetric and *EBSD* measurements and indicates that recrystallization occurred at the temperature higher than 400 °C and finished at about 600 °C. Therefore, the study of texture evolution confirms the results obtained so far; however, it does not provide additional information regarding the recovery process, during which no change in grain orientation is observed.

*4.1.4. Microhardness*

Similar conclusions as in the case of *EBSD* measurements and measurements of texture can be drawn from an analysis of the hardness evolution as a function of annealing temperature (Fig. 5). The hardness of the non-annealed sample and those annealed at 200 °C and 400 °C is almost identical (the effects of recovery are not seen), and a significant decrease of hardness is observed in the temperature range 400 °C–600 °C, due to the recrystallization process. Moreover, the hardness measurements confirm that 50% of material is recrystallized at about a temperature of 500 °C, as was also observed in the DSC experiment.

*4.1.5. Diffraction measurements of the peak width and residual stresses*

The tests which are one of the main goals of the present study concern the variation of the first and the second order stresses due to thermal treatment. The nonlinear $sin^2\psi$ method used in this paper was tested previously for cold rolled and annealed samples (see [13]). Fig. 6 shows the experimental and theoretical plots of $<a(\phi, \psi)>_{\{hkl\}}$ vs. $sin^2\psi$ for the 211 reflection and various annealing temperatures, measured using Cr radiation (the conditions are given in Table 2). It was found that at 200 °C the slope of graphs decreased, indicating a reduction of the first order stress. At 400 °C the nonlinearities on the $<a(\phi, \psi)>_{\{hkl\}}$ vs. $sin^2\psi$, caused due to the plastic mismatch stresses, also started to decrease and they completely disappeared at 600 °C.

The quantitative evolution of the stress as a function of annealing temperatures is shown in Fig. 7. In this figure the main components of the first order stress $\sigma^I_{ij}$ are presented together with the average equivalent von Mises stress $\sigma^{IIg(pi)}_{eq}$ calculated by applying Eq. (7) for the plastic mismatch second order stress (Fig. 7a). In Fig. 7b, the second order equivalent stress $\sigma^{IIg(pi)}_{eq}$ is compared with the equivalent first order stress $\sigma^I_{eq}$, calculated also from Eq. (7) but for the $\sigma^I_{ij}$ stresses.

Analyzing the quantitative results of stress analysis, it can be observed that the plastic incompatibility stress in the cold-rolled ferritic sample was twice as small compared to the macroscopic stress, c.f. the von Mises measure shown in Fig. 7b. After annealing at 100 °C, the state of stress does not change. Annealing at 200 °C led to an important reduction in the first order stress $\sigma^I_{eq}$, while the plastic incompatibility stress $\sigma^{IIg(pi)}_{eq}$ did not change. Only at 400 °C are the substantial decrease in stress of the second order $\sigma^{IIg(pi)}_{eq}$ and the subsequent relaxation of macrostress $\sigma^{IIg(pi)}_{eq}$ observed. The latter effect can be correlated with the strong decrease of the diffraction peak width (*FWHM*) visible in Fig. 8, as well as with a noticeable exothermic process observed in the calorimetric measurements (Fig. 2).

It was found that the stresses of the first ($\sigma^I_{eq}$) and the second order ($\sigma^{IIg(pi)}_{eq}$) completely relaxed in the samples annealed at temperatures of 600 °C and 800 °C, for which the recrystallization was finished. A small value of about 20 MPa of the residual stress $\sigma^I_{eq}$ was caused by the stress gradient occurring during cooling of the specimen after annealing. It can be concluded that stress measurements showed the highest sensitivity on microstructure evolution in comparison with the previously used research techniques, and provided new information on the processes occurring in the sample. They showed that thermal processes cause macroscopic stress relaxation even during annealing at so low a temperature as 200 °C. Relaxation of the first order stresses proceeds during the recovery. Also, as has been shown, the plastic second order mismatch stress relaxed at a higher temperature than the first order stress, i.e., around 400 °C. At this temperature a considerable reduction of the crystal lattice defects occurred, causing a slight decrease of the diffraction peak width. Moreover, at this stage the recovery process caused the heat release which was registered in the calorimetric measurements. One can also state that, after recrystallization (at 600 °C), the internal stresses produced during the cold rolling process are fully relaxed.

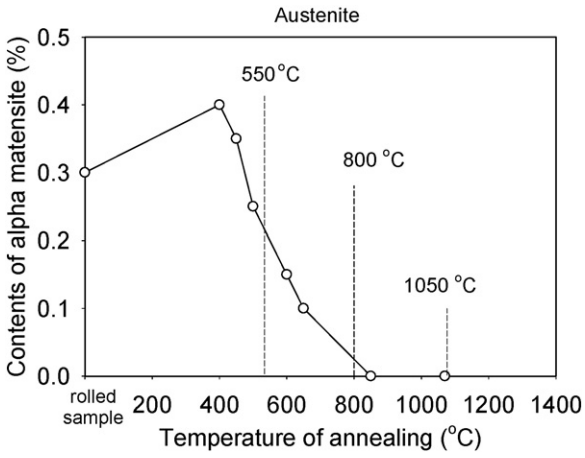


**Fig. 10.** Content of martensite measured for the investigated austenite sample cold rolled and annealed during 120 min (magnetization measurements).

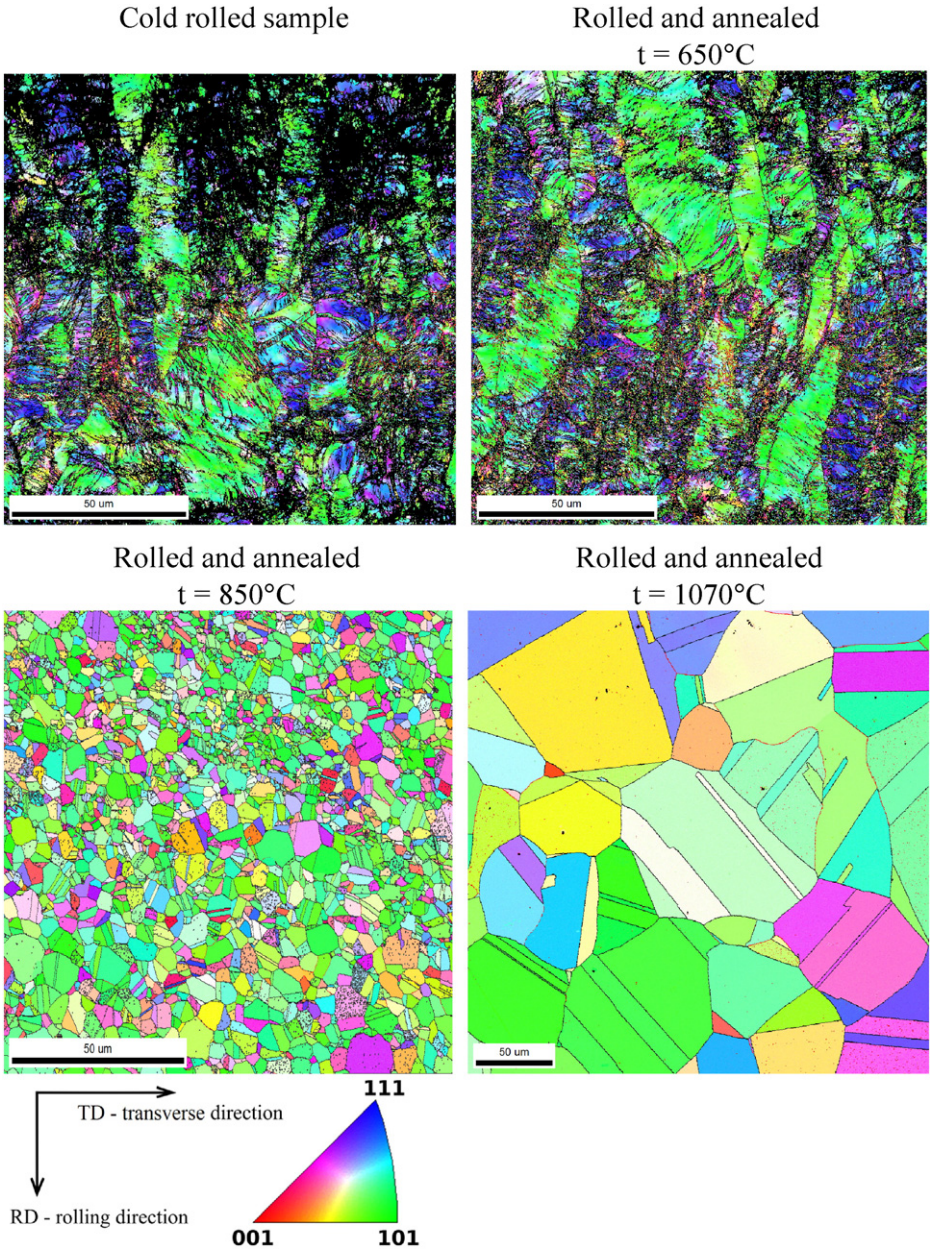


**Fig. 12.** The orientation maps obtained by *EBSD* for cold rolled (70% of reduction) and isothermally annealed austenitic stainless steel.

*4.2. Austenitic stainless steel*

Similarly as for ferritic steel, calorimetric measurements were performed for cold rolled austenitic stainless steel (AISI 316L) with use of the differential scanning calorimeter DSC Netzsch 404 F1 Pegasus. In addition, the *EBSD* maps (FEI Versa 3D Dual Beam FIB/SEM), Vickers hardness, crystallographic texture and residual stresses were determined. Moreover, variation of the ferromagnetic phase fraction (martensite) was characterized by the magnetization measurements using a Permeameter MP-100 produced by R&J Measurement.

*4.2.1. Phase transformations — calorimetric, magnetic and X-ray diffraction measurements*

The results of the calorimetric measurement performed for the cold rolled austenitic stainless steel (see Fig. 9) show that the process of energy release during heating is much more complicated compared to the ferritic steel (c.f. Figs. 9 and 2). In addition to the recovery and recrystallization processes, the phase transformations such as precipitation of carbides, the intermetallic phases $\chi$, $\sigma$ and $\eta$, and the reverse martensitic transformation [26] must also be considered in austenitic stainless steels. Such precipitation processes – which are exothermic transformations – were described for example by Weiss and Stickler [27], Wasnik et al. [28] and Plaut et al. [29]. The precipitation of intermetallic phases requires an annealing time much longer than the isothermal annealing time of 2 h which was used in the present study. Therefore, precipitation of this kind should have no influence on the results of the calorimetric measurements as well as other studies carried out in this work. However, reverse martensitic transformation [30,31] may occur in the examined steel AISI 316L. A small content ca. 0.3% of $\alpha$ martensite was estimated in the initial sample from the magnetic measurements. It was found that the fraction of martensitic phase decreased rapidly with the temperature of annealing (Fig. 10). This result shows that the endothermic effect between 400 °C and 750 °C observed in the calorimetric measurement (Fig. 9) can be interpreted as the reverse martensitic transformation.

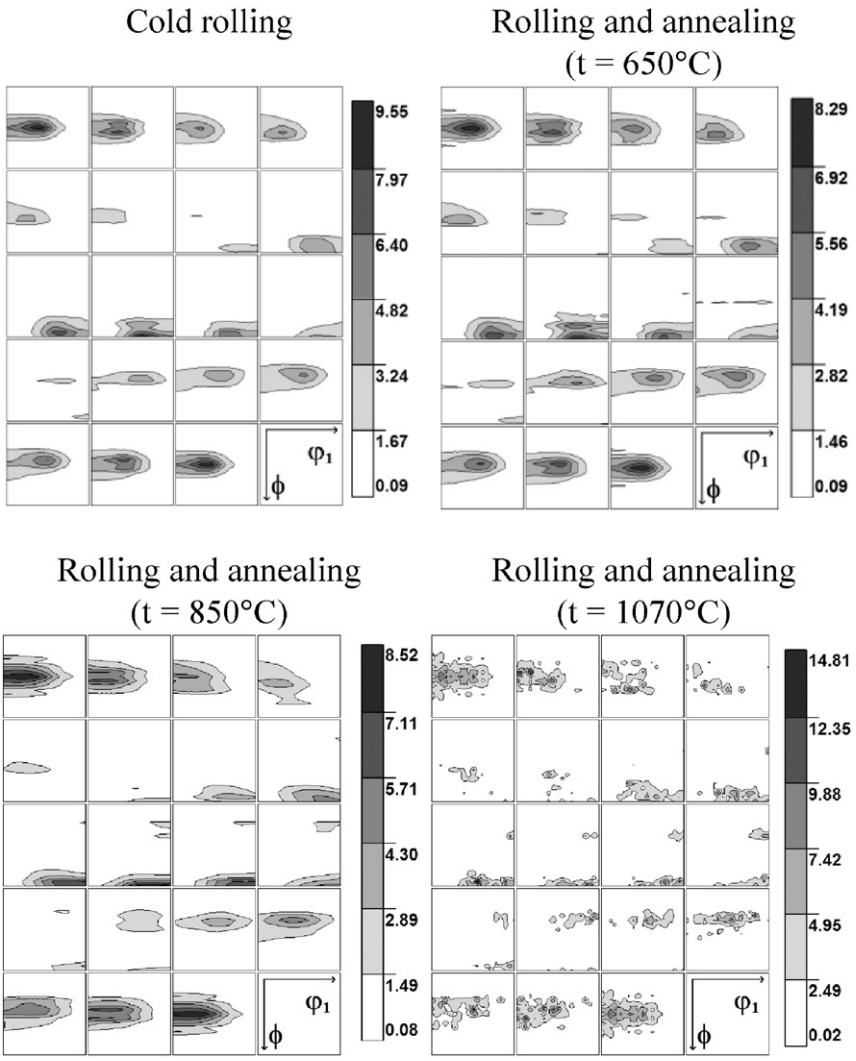


**Fig. 13.** Orientation distribution functions obtained for samples of austenitic stainless steel, cold rolled and annealed at different temperatures (sections through Euler space displaces with increment of 5° along axis $\varphi_2$ are shown [21]).

Analyzing Fig. 9, it can be concluded that the first exothermic transformation, occurring at a temperature of about 550 °C, can be caused by the precipitation of $M_{23}C_6$ type carbides [28]. The rapid evolution of carbides in the steels type 316L, undeformed or after small plastic deformation, occurs at temperatures of 550 °C–800 °C, however a large deformation of the material speeds up the process significantly [27]. The four steps of nano-precipitation process occurring in the grain boundaries were described by Wasnik et al. [28]. In the austenite studied in this work, the precipitation of the $M_{23}C_6$ carbides was confirmed by X-ray diffraction measurements. As seen in Fig. 11, the diffraction peaks corresponding to the presence of $M_{23}C_6$ carbide appear for the sample annealed at 500 °C and slowly disappear with increasing temperature of the annealing.

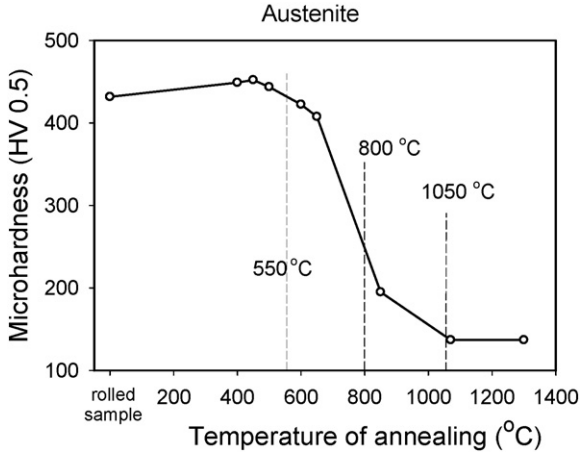


**Fig. 14.** Vickers microhardness measured for samples of austenitic stainless steel cold rolled and annealed at different temperatures. The dashed lines depict characteristic temperatures found in the calorimetric measurements, c.f. Fig. 9.

According to Spruiell et al. [32], the recrystallization in the steel 316L proceeds slowly and its beginning is much delayed. Indeed, the calorimetric measurements (Fig. 9), show a maximum of exothermic peak at 800 °C, which is overlapped by the next peak with a maximum at about 1050 °C, i.e., the exothermic processes at these temperatures may result from the recrystallization which occurs slowly in two stages at high temperatures.

In the present study, the thermal effect linked with the recovery process was not clearly observed in the calorimetric studies. This indicates that the recovery is slow and accompanied by the releasing of a small amount of heat. The reason for the decreasing of the recovery rate is a small value of the stacking fault energy for 316L steel (*SFE* is about 28 $10^{-3}$ J/m$^2$, according to [32,33]). In alloys having a low stacking fault energy, the dislocations form relatively wide dislocation ribbons

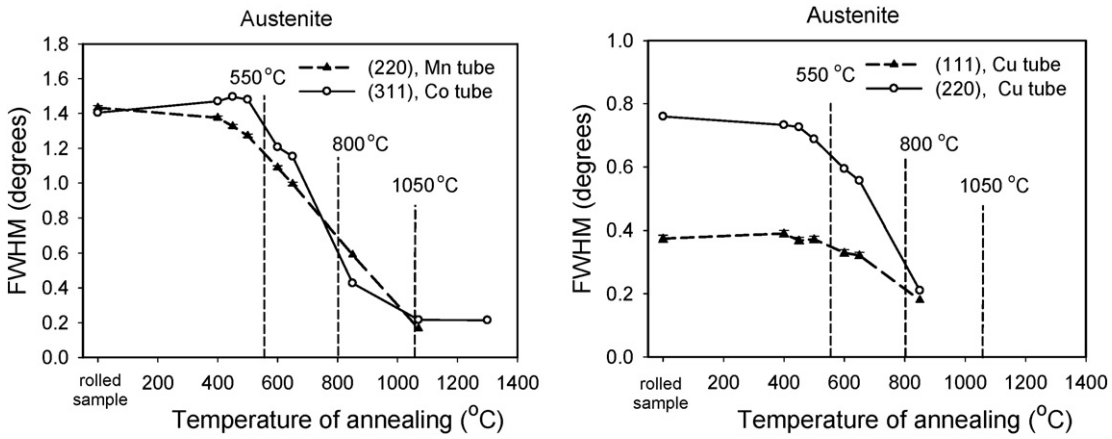


**Fig. 15.** Changes of peak widths versus annealing temperature determined for the cold rolled austenitic samples.

composed of partial dislocations separated by the stacking faults. This prevents or significantly impedes phenomena such as climbing and slipping of the lateral dislocations, which in turn slows down the recovery process [5].

*4.2.2. Examination of the microstructure using EBSD technique*

The study of the microstructure performed for the deformed and annealed austenitic stainless steel (see *EBSD* maps in Fig. 12) confirmed the results of the calorimetric measurements. The thicker black lines on the orientation maps represent boundaries between separate grains with lattice misorientation greater or equal to 10°, while thin red lines are drawn for low angle boundaries with misorientation of crystallographic lattice in the angular range of 2°–15°. It was found that in the case of the cold rolled austenitic stainless steel with a low value of *SFE* the *EBSD* orientation maps are very difficult to measure. An analysis of the Kikuchi bands failed for this sample in the predominant areas due to a high density of lattice defects density. A similar situation also occurred in the case of the sample annealed at 400 °C, but for the material annealed at 650 °C the areas of identified orientations slightly increased due to a reduction of defects density. This may indicate that in the sample annealed at 650 °C the process of recovery occurred.

A fundamental change of microstructure occurred after isothermal annealing at 850 °C, i.e., at a temperature slightly higher that the exothermic effect determined in the *DSC* measurements with the peak temperature at 800 °C. The grains significantly elongated in the rolling direction (*RD*) after cold rolling transformed into smaller, approximately equiaxed ones, characteristic for the primary recrystallization process which occurs in metals containing precipitates of the other phases [5] (Fig. 12, t = 850 °C). The sample annealed at 1070 °C exhibited very large recrystallized grains with the distinct recrystallization twins (Fig. 12, t = 1070 °C). Such large grains indicate the advanced process of recrystallization growth. The last result corresponds to the calorimetric measurement, showing exothermic effect with the maximum at t = 1050 °C. It is also consistent with the literature, e.g., similar austenitic grain growth at a temperature of about 1100 °C was observed by Plaut [29]. The relatively high value of recrystallization temperature obtained for the cold rolled AISI 316L steel was also determined by other authors. For example, Donadille et al. [34] found that full recrystallization of this steel subjected to the cold rolling reduction of 40% requires annealing during 2 h at a temperature of 900 °C. According to Herrera et al. [31] 50% of the volume of the same steel but cold rolled up to a reduction of 90%, recrystallizes after annealing at 800 °C during 1 h.

Finally, the presence of carbides in the annealed samples was confirmed by the *EBSD* image quality maps and indexed Kikuchi patterns showing the $M_{23}C_6$ and $M_7C_3$ carbides in the deformed and annealed material.

*4.2.3. Crystallographic texture*

Fig. 13 provides *ODFs* for cold rolled and subsequently annealed samples calculated from pole figures measured using the Mn X-ray radiation (conditions are given in Table 2). The texture characteristic for the cold rolled *f.c.c.* metals with low value of *SFE* (called *brass texture*) was determined for the deformed material. The texture almost did not change during annealing, even when recrystallization occurred. After recrystallization at 850 °C the measured *ODF* was practically the same as directly after rolling and, what is more, the major components of *ODF* did not change even after annealing at 1070 °C, corresponding to significant growing of the recrystallized grains. It can be also observed that the cubic component of the texture, usually characteristic for recrystallization texture of rolled *f.c.c.* metals [5], did not appear. The only important change that occurred at 1070 °C is a significant perturbation of the *ODF* contours, resulting from a smaller number of crystallites participating in the diffraction (due to grain growth confirmed by *EBSD* measurements, c.f. Fig. 12). It can be concluded that in the tested samples of austenitic stainless steel, the significantly delayed recrystallization process leads to growing of the grains having unchanged orientations, i.e., the texture is the same as in the cold rolled material.

As it was stated by Chowdhury et al. [35], the reason of the retention of rolling texture and delay of the recrystallization process in annealed cold rolled 316L steel remains unclear. Such behavior is commonly attributed to the strong solute effect of Mo. It was suggested by Engler [36] that the recrystallization is delayed due to the retardation of the nucleation rate as well as hindrance to the migration of high-angle grain boundaries. Alloying elements (in this case Mo) in the solid solution strongly influence the progress of recrystallization by significantly slowing down the motion of grain boundary. Another observation presented by Donadille et al. [34] shows that the retention of the rolling texture is caused by the discontinuous recrystallization and lack of interaction between recrystallization front and precipitating particles. The retention of the rolling texture during annealing may also be explained by the extended recovery, causing the deformed substructure to undergo homogeneous recrystallization without nucleation [31].

*4.2.4. Microhardness*

Changes in hardness of austenitic stainless steel in the function of annealing temperature (Fig. 14) confirm the results of calorimetric and microscopic measurements. It can be concluded that during annealing up to temperature 500 °C hardness of the material does not change significantly. It can be also observed that for temperatures lower than 500 °C, the evolution of hardness is not correlated with significantly decreasing martensite contents (c.f. Figs. 10 and 14). A slight decrease in hardness for annealing temperatures of 600 °C and 650 °C can be explained by recovery as well as reverse martensite transformation. A

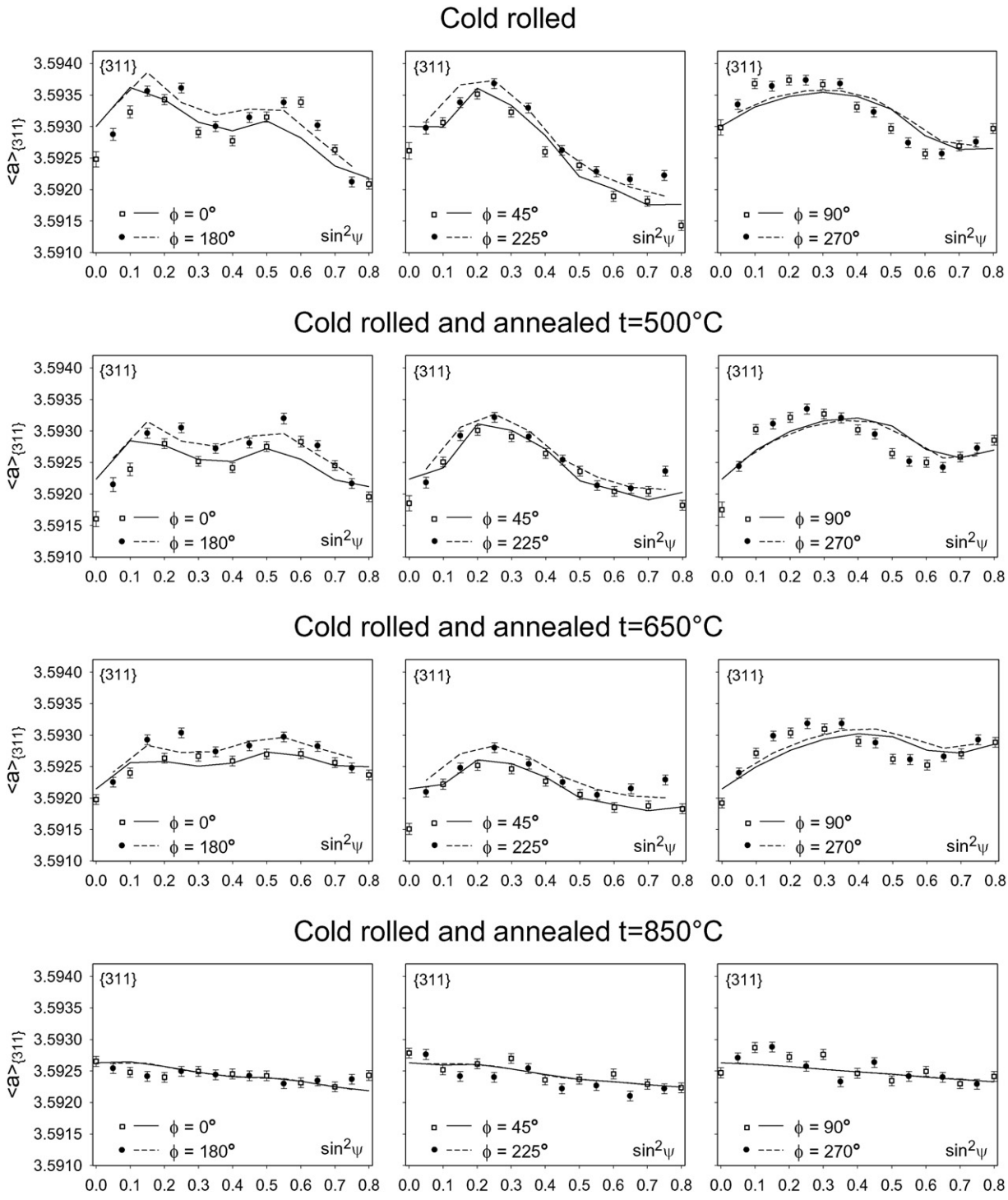


**Fig. 16.** The results of the theoretical lines fitting to the experimental plots ($<a(\phi,\psi)>_{\{hkl\}}$ vs. $sin^2\psi$) for the austenitic stainless steel samples rolled to the reduction of 70% and annealed at different temperatures (nonlinear $sin^2\psi$ method). The results for the 311 reflection are presented.

significant decrease of the hardness after annealing at 850 °C corresponds to the recrystallization, and then grains growth, after annealing at a temperature of 1070 °C, caused a slight decrease in hardness (c.f. *EBSD* maps in Fig. 12).

*4.2.5. Diffraction measurements of the peak width and residual stresses*

The Mn (c.f. Table 2), Cu ($\lambda_{K\alpha1} = 1.54060$ Å and $\lambda_{K\alpha2} = 1.54443$ Å) and Co ($\lambda_{K\alpha1} = 1.78897$ Å and $\lambda_{K\alpha2} = 1.79285$ Å) X-ray radiation were used to determine the variation of the width of the diffraction peaks. The results shown in Fig. 15 are fully correlated with the evolution of microhardness (Fig. 14). The only difference is a more significant decrease in the *FWHM* compared to the small changes in the microhardness during recovery, i.e., at the temperature range between 600 °C and 650 °C. It can be concluded that microhardness of the austenitic sample is mostly influenced by the dislocation density, which also affects the width of the diffraction peaks.

The results of residual stress measurements using X-ray diffraction (Mn tube — see Table 2) are shown in Fig. 16, which summarizes the theoretical and experimental curves of $<a(\varphi,\psi)>_{\{hkl\}}$ vs. $sin^2\psi$ corresponding to different temperatures of annealing [13]. The obtained

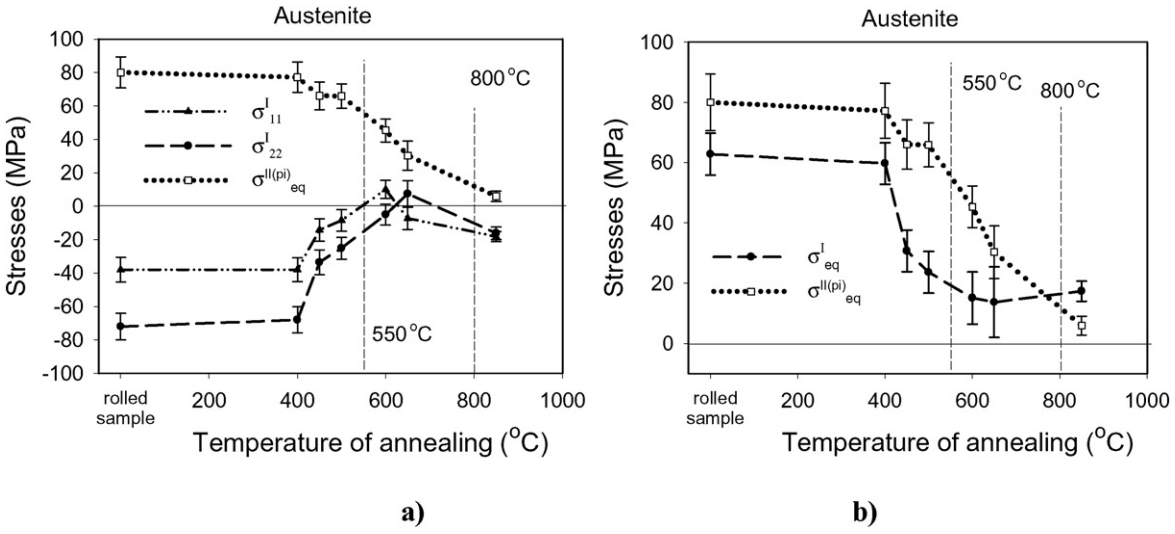


**Fig. 17.** The evolution of residual stress in the investigated samples of austenite in function of annealing temperature: a) components of the first order macrostress $\sigma^{I}_{ii}$ and the average von Mises plastic mismatch stress $\sigma^{IIg(pi)}_{eq}$, b) von Mises stresses calculated for the first ($\sigma^{I}_{eq}$) and the plastic incompatibility ($\sigma^{IIg(pi)}_{eq}$) stresses.

results indicate that the relaxation of the macrostresses proceeded at 500 °C (the slopes of plots decreased), while the plastic mismatch stresses started to relax at higher temperatures as the non-linearity of curves decreased significantly at 650 °C.

The main components of the macroscopic stress tensor and average equivalent von Mises stress (Eq. (7)) are presented in Fig. 17a, while the evolution of the equivalent von Mises stresses calculated for both types of the stress are shown in Fig. 17b. For the cold-rolled austenitic stainless steel, the macroscopic stress $\sigma^{I}_{eq}$ was smaller than the plastic incompatibility stress $\sigma^{IIg(pi)}_{eq}$, unlike in the case of ferritic steel (Fig. 7). For the annealed samples, residual stresses practically do not change until the temperature of 400 °C.

At a temperature of 450 °C a significant reduction in the first order stress $\sigma^{I}_{eq}$ occurred and a slight decrease in the plastic stress mismatch $\sigma^{IIg(pi)}_{eq}$ could be noticed. A distinct reduction of the stress $\sigma^{IIg(pi)}_{eq}$ is visible for the sample annealed at 600 °C. For this sample, the macroscopic stress decreased to a small value probably corresponding to the stresses generated during cooling of the sample after annealing process.

Analyzing Figs. 17, 14 and 15 it can be concluded that the decrease in the plastic mismatch stress $\sigma^{IIg(pi)}_{eq}$ correlates well with the changes in microhardness of samples and with changes in the defects density, indicated by the *FWHM* evolution. On the contrary, the first order stress $\sigma^{I}_{eq}$ relaxed at lower temperatures, indicating the start of the recovery process similarly as for the ferritic steel. The latter effect was not seen in the measurements performed in this work using the other experimental techniques.

### 4.3. Comparison of processes occurring in the studied steels

Comparing the processes in both studied steels, it can be concluded that the recovery process occurs significantly slower in the austenite than in the ferrite steel. Because of the significantly delayed recrystallization in the austenitic sample both the slow softening of the material and a decrease in the dislocation density during annealing were observed. In the case of ferritic steel, peak width decreased rapidly just before recrystallization, indicating the intensification of the recovery process. However, the reduction in dislocation density (which results in the reduction of the diffraction peak width) was not associated with the decrease in hardness of the ferritic steel.

The different intensities of the recovery process can be explained through two types of dislocation movement: nonconservative (climb) and conservative (slip/twinning). A higher value of the stacking fault energy leads to more difficult dissociation of perfect dislocation into two partial dislocations, therefore it facilitates dislocation climb and cross slip. In metals such as ferrite the recovery process is separated from the recrystallization as it occurs at lower temperatures. In metals with a low value of *SFE* such as the investigated austenitic stainless steel, climb and cross slip are restricted because of dislocation dissociation. Therefore, the recovery occurs at higher temperatures, often simultaneously with the recrystallization [5]. However, in the case of the studied austenitic stainless steel, a significant delay of recrystallization leads to the separation of both processes.

The recovery process changes the diffraction peak width, and in some cases influences the hardness of the sample. However, these changes are often quite small and difficult to observe. Only residual stress measurement clearly shows the processes which can be considered as the beginning of recovery. In the studied samples a very distinct stress relaxation, preceding such effects as diffraction peak broadening or material softening, was observed. Moreover, in all cases the relaxation of the macrostress $\sigma^{I}_{ij}$ appears at lower temperatures in comparison with the release of the plastic mismatch stress $\sigma^{IIg(pi)}_{ij}$. It follows that the relaxation of these stresses during recovery should be explained in a different way. Macrostresses ($\sigma^{I}_{ij}$) caused by the interaction of large volumes of the sample can relax at lower temperatures, e.g., due to the polygonization effect. During this process, the thermally activated motion of dislocations leads to the formation of low angle boundaries dividing the polycrystalline grains into subgrains. This process does not cause a decrease in the dislocation density large enough to decrease significantly the diffraction peak width. In the studied samples a considerable relaxation of macrostresses ($\sigma^{I}_{ij}$) occurs at 200 °C for the ferritic steel and at 450 °C for austenitic stainless steel, while the changes of the peak width was not observed at these temperatures.

Plastic mismatch stresses $\sigma^{IIg(pi)}_{ij}$ relax in a different way. They begin to decrease at a higher temperature and relax slower than macrostresses $\sigma^{I}_{ij}$ (c.f. Figs. 7 and 17). Strongly anisotropic second order stress ($\sigma^{IIg(pi)}_{ij}$) is generated by a mismatch between grains having different lattice orientations and separated by the high angle boundaries. To relax such stresses, higher temperatures allowing more significant rebuilding of the dislocation microstructure, including the annihilation of dislocations, are required. Such an effect is clearly visible for all the investigated materials, for which the relaxation of $\sigma^{IIg(pi)}_{ij}$ was associated with a slow and continuous decrease in dislocation density, as was evidenced by the decrease of the diffraction peak width.

Interesting effects were also observed at the beginning of the recrystallization. For both investigated steels macrostresses $\sigma^{I}_{ij}$ relax entirely, and second order stresses $\sigma^{IIg(pi)}_{ij}$ almost entirely before recrystallization.

As mentioned previously, in the case of ferritic steel (comparatively high value of *SFE*) recovery occurs at quite a low temperature due to the high mobility of dislocations. On the other hand, despite the slow recovery in the austenite (low value of *SFE*), the stresses have enough time to relax before much delayed recrystallization.

The beginning of recrystallization is associated with decrease of the *FWHM* up to the minimum value resulting from the apparatus factor and finite size of the grains. A little more advanced recrystallization causes a significant reduction in the material hardness. In the case of ferritic steel, the crystallographic texture also changes at the beginning of recrystallization. This phenomenon, however, is not a general rule, as seen in the case of austenite for which the texture does not change even during advanced recrystallization.

## 5. Discussion and conclusions

Different methodologies used to study changes occurring during the processes of recovery and recrystallization show the evolution of various properties of the samples. Only a comprehensive study using multiple methods may provide a full picture of the processes occurring during thermal treatment of the studied materials. The *DSC* methods allow for determining the temperature ranges in which the exothermic processes associated with the recovery and recrystallization occur. It is difficult, however, to separate these processes from structural transformations, e.g., precipitation of other phases. Moreover, it is not easy to notice the recovery process as it is accompanied by the release of a small amount of heat taking place gradually over a wide range of temperature. On the basis of microhardness measurement, the recrystallization temperature can be determined, and in some cases these measurements also allow for the observation of the advanced recovery process, as in the case of the studied austenitic stainless steel.

The effect of recrystallization is visible on the *EBSD* orientation maps due to clear microstructure changes, but the recovery process is not seen in this investigation. The recovery does not noticeably affect the crystallites orientation, but usually the texture changes in the course of recrystallization. The exception was austenitic stainless steel examined in this work. The recovery may be detected by measuring the diffraction peak width which decreases as a result of annihilation of defects and evolution of their structure in the material.

An important result of this work is the observation that the residual stresses can be considered as the phenomenon most sensitive to small changes in the microstructure. Their relaxation occurs at the beginning of recovery at temperatures at which other techniques used in this work cannot detect any microstructure changes. Moreover, as has been demonstrated, only the stress analysis allowed for distinguishing the two stages of the recovery process. During the first step, the first-order stress $\sigma_{ij}^{I}$ relaxes due to slight modification of the dislocation structure. In the following step, the relaxation of the plastic mismatch stress ($\sigma_{ij}^{IIg(pi)}$) is caused by the substantial reconstruction of the microstructure due to annihilation and re-arrangement of the dislocations.

## Acknowledgments

This work was financed by the grants from Polish National Scientific Center (*NCN*): UMO-2011/03/N/ST8/04058 and DEC-2013/11/B/ST3/03787. The support of the Polish Ministry of Science and Higher Education (*MNiSW*) is also acknowledged.

## References

[1] I.C. Noyan, J.B. Cohen, Residual Stress — Measurement by Diffraction and Interpretation, Springer–Verlag, New York–Berlin–Heidelberg–London–Paris–Tokyo, 1987.
[2] V. Hauk, Structural and Residual Stress Analysis by Nondestructive Methods, Elsevier Science B.V., Amsterdam, 1997.
[3] M.E. Fitzpatrick, A. Lodini, Analysis of Residual Stress by Diffraction Using Neutron and Synchrotron Radiation, first ed. CRC Press, 2003.
[4] G. Maeder, J.L. Lebrun, J.M. Sprauel, Present possibilities for the X-ray diffraction method of stress measurement, Non Destr. Test Int. 14 (1981) 235–248.
[5] F.J. Humphreys, M. Hatherly, Recrystallization and Related Annealing Phenomena, second ed. Elsevier, Amsterdam, Boston, Heidelberg, London, New York, Oxford, Paris, San Diego, San Francisco, Singapore, Sydney, Tokyo, 2004.
[6] A. Baczmański, K. Wierzbanowski, P. Lipiński, R.B. Helmholdt, G. Ekambaranathan, B. Pathiraj, Examination of the residual stress field in plastically deformed polycrystalline material, Philos. Mag. A 69 (1994) 437–449.
[7] A. Baczmański, C. Braham, W. Seiler, Microstresses in textured polycrystals studied by multireflection diffraction method and self consistent model, Philos. Mag. A 83 (2003) 3225–3246.
[8] A. Baczmański, P. Lipiński, A. Tidu, K. Wierzbanowski, B. Pathiraj, Quantitative estimation of incompatibility stresses and elastic energy stored in ferritic steel, J. Appl. Crystallogr. 41 (2008) 854–867.
[9] S. Wroński, A. Baczmański, R. Dakhlaoui, C. Braham, K. Wierzbanowski, E. Oliver, Determination of stress field in textured duplex steel using TOF neutron diffraction method, Acta Mater. 55 (2007) 6219–6233.
[10] D. Gloaguen, M. François, R. Guillen, Mesoscopic residual stresses of plastic origin in zirconium: interpretation of X-ray diffraction results, J. Appl. Crystallogr. 37 (2004) 934–940.
[11] D. Gloaguen, T. Berchi, E. Girard, R. Guillen, Measurement and prediction of residual stresses and crystallographic texture development in rolled zircaloy–4 plates: X-ray diffraction and the self-consistent model, Acta Mater. 55 (2007) 4369–4379.
[12] U. Welzel, J. Ligot, P. Lamparter, A.C. Vermeulen, E.J. Mittemeijer, Stress analysis of polycrystalline thin films and surface regions by X-ray diffraction, J. Appl. Crystallogr. 38 (2005) 1–29.
[13] R. Wawszczak, A. Baczmański, C. Braham, W. Seiler, M. Wróbel, K. Wierzbanowski, A. Lodini, Residual stress field in steel samples during plastic deformation and recovery processes, Philos. Mag. 91 (2011) 2263–2290.
[14] P. Franciosi, M. Berveiller, A. Zaoui, Latent hardening in copper and aluminium single crystals, Acta Metall. 28 (1980) 273–283.
[15] P. Lipinski, M. Berveiller, Elastoplasticity of micro-inhomogeneous metals at large strains, Int. J. Plast. 5 (1989) 149–172.
[16] P. Lipinski, M. Berveiller, E. Reubrez, J. Morreale, Arch. Appl. Mech. 65 (1995) 291–311.
[17] P. Zattarin, A. Baczmański, P. Lipiński, K. Wierzbanowski, Modified self-consistent model for time independent plasticity of polycrystalline material, Arch. Metall. Mater. 45 (2000) 163–184.
[18] T. Leffers, Computer simulation of the plastic deformation in face-centred cubic polycrystals and the rolling texture derived, Phys. Status Solidi 25 (1968) 337–343.
[19] K. Wierzbanowski, M. Wroński, A. Baczmański, B. Bacroix, P. Lipiński, A. Lodini, Problem of lattice rotation due to plastic deformation. Example of rolling of f.c.c materials, Arch. Metall. Mater. 56 (2011) 575–584.
[20] K. Wierzbanowski, J. Jura, W.G. Haije, R.B. Helmholdt, F.C.C. rolling texture transitions in relation to constraint relaxation, Cryst. Res. Technol. 27 (1992) 513–522.
[21] H.J. Bunge, Texture Analysis in Material Science — Mathematical Methods, Butterworths & Co., London, Boston, 1982.
[22] J.S. Kallend, U.F. Kocks, A.D. Rollett, H.-R. Wenk, Operational texture analysis, Mater. Sci. Eng. A 132 (1991) 1–11.
[23] P. Thompson, D.E. Cox, J.B. Hastings, Rietveld refinement of Debye–Scherrer synchrotron X-ray data from $Al_2O_3$, J. Appl. Crystallogr. 20 (1987) 79–83.
[24] K. Inal, P. Gergaud, M. François, J.-L. Lebrun, Stress analysis in a duplex steel. X-ray diffraction methodologies of macro and pseudo-macro stress analysis in a textured duplex stainless steel, Scand. J. Metall. 28 (1999) 139–150.
[25] G. Simmons, H. Wang, Single Crystal Elastic Constants and Calculated Aggregate Properties, A Handbook, The MIT Press, Cambridge, Massachusetts, 1971.
[26] E. Dryzek, M. Sarnek, M. Wróbel, Reverse transformation of deformation-induced martensite in austenitic stainless steel studied by positron annihilation, J. Mater. Sci. 49 (2014) 8449–8458.
[27] B. Weiss, R. Stickler, Phase instabilities during high temperature exposure of 316 austenitic stainless steel, Metall. Trans. 3 (1972) 851–866.
[28] D.N. Wasnik, G.K. Dey, V. Kain, I. Samajdar, Precipitation stages in a 316L austenitic stainless steel, Scr. Mater. 49 (2003) 135–141.
[29] R.L. Plaut, C. Herrera, D.M. Escriba, P.R. Rios, A.F. Padilha, A short review on wrought austenitic stainless steels at high temperatures: processing, microstructure, properties and performance, Mater. Res. 10 (2007) 453–460.
[30] S.K. Ghosh, P. Mallick, P.P. Chattopadhyay, Effect of reversion of strain induced martensite on microstructure and mechanical properties in an austenitic stainless steel, J. Mater. Sci. 46 (2011) 3480–3487.
[31] C. Herrera, R.L. Plaut, A.F. Padilha, Microstructural refinement during annealing of plastically deformed austenitic stainless steels, Mater. Sci. Forum 550 (2007) 423–428.
[32] J.E. Spruiell, J.A. Scott, C.S. Ary, R.L. Hardin, Microstructural stability of thermal-mechanically pretreated type 316 austenitic stainless steel, Metall. Mater. Trans. 4 (1973) 1533–1544.
[33] S.W. Yang, J.E. Spruiell, Cold-worked state and annealing behaviour of austenitic stainless steel, J. Mater. Sci. 17 (1982) 677–690.
[34] C. Donadille, R. Valle, P. Dervin, R. Penelle, Development of texture and microstructure during cold-rolling and annealing of F.C.C. alloys: example of an austenitic stainless steel, Acta Metall. 37 (1989) 1547–1571.
[35] S.G. Chowdhury, S. Das, B. Ravikumar, P.K. De, Twinning-induced sluggish evolution of texture during recrystallization in AISI 316L stainless steel after cold rolling, Metall. Mater. Trans. A 37 (2006) 2349–2359.
[36] O. Engler, On the origin of the *R* orientation in the recrystallization textures of aluminum alloys, Metall. Mater. Trans. A 30 (1999) 1517–1527.